Supplementary Information Of Real-Time and High-Fidelity Non-Line-of-Sight Imaging

Jianyu Wang[1,†], Leping Xiao[2,3 †], Shiwei Wu[4], Yuran Wang[2,3], Zuoqiang Shi[1,5], Lingyun Qiu[1,5], Xing Fu[2,3,*], Xiangyang Ji[6,*]

[1]Yau Mathematical Sciences Center, Tsinghua University,Beijing, 100084, China
[2]Department of Precision Instrument, Tsinghua University, Beijing, 100084, China
[3]State Key Laboratory of Precision Space-time Information Sensing Technology, Beijing, 100084, China
[4]Qiuzhen College, Tsinghua University, Beijing, 100084, China.
[5]Yanqi Lake Beijing Institute of Mathematical Sciences and Applications, Beijing, 101408, China.
[6]Department of Automation, Tsinghua University, Beijing, 100084, China.
[*]Corresponding author: fuxing@tsinghua.edu.cn, xyji@tsinghua.edu.cn
[†]These authors contributed equally to this work.

S.1 Supplementary Methods

S.1.1 Iterative scheme of the reconstruction pipeline

In this subsection, we present the full details of the iterative scheme and its implementation. In the main text, we have formulated high-quality and efficient NLOS imaging under general scenarios and measurement patterns as the following optimization problem:

$$\arg\min_{a,d} \sum_{s\in S} \|\mathcal{F}_s(a,d) - \boldsymbol{\phi}_s\|_2^2 + \lambda_{ALB}\|a\|_1 + \lambda_{TV}\|\nabla a\|_1 + \lambda_{SUPP}\|\mathbb{I}[a>0] - \mathbb{I}[d>0]\|_1, \tag{S.1}$$

where a and d represents the two-dimensional albedo and depth functions, respectively. The variable s denotes the scale parameter that controls the spread of the wavefront, and S is the set of all used scale parameters. $\mathcal{F}_s$ and ϕ_s denote the forward operator and aggregated measurement associated with parameter s. The term λ_{ALB}, λ_{TV} and λ_{SUPP} are hyperparameters that balance the effects of the respective regularization terms. The operator ∇ denotes the gradient operator and the operator $\mathbb{I}$ denotes the indicator function. Besides, $\|\cdot\|_1$ and $\|\cdot\|_2$ denote the L_1 and L_2 norm, respectively.

We solve this optimization problem using the split Bregman method [1]. Since the gradient of the support prior is difficult to compute, we treat it as an independent subproblem during the iterative process. By introducing the auxiliary variables a_o, b_a, $\boldsymbol{a}_{TV}$ and $\boldsymbol{b}_{TV}$, the objective function then becomes:

$$\sum_{s\in S} \|\mathcal{F}_s(a,d) - \phi_s\|_2^2 + \lambda_{ALB}\|a_o\|_1 + \frac{\mu_{ALB}}{2}\|a_o - a - b_a\|_2^2 + \lambda_{TV}\|a_{TV}\|_1 + \frac{\mu_{TV}}{2}\|\boldsymbol{a}_{TV} - \nabla a - \boldsymbol{b}_{TV}\|_2^2, \tag{S.2}$$

where μ_{ALB} and μ_{TV} are introduced hyperparameters. Then the problem can be solved through several subproblems. Next, we introduce the approach for solving each subproblem. In the substep of updating the two-dimensional functions, we solve the following optimization problem:

$$\arg\min_{a,d} \sum_{s\in S} \|\mathcal{F}_s(a,d) - \phi_s\|_2^2 + \frac{\mu_{ALB}}{2}\|a_o - a - b_a\|_2^2 + \frac{\mu_{TV}}{2}\|\boldsymbol{a}_{TV} - \nabla a - \boldsymbol{b}_{TV}\|_2^2. \tag{S.3}$$

Although this subproblem is differentiable due to the variable splitting, we currently use PyTorch's automatic differentiation to simplify implementation. However, this adds approximately 50% overhead to the total computational time. To improve the efficiency of the reconstruction pipeline, we plan to explicitly implement the gradient computation in future work. In the substep of updating a_o, the following problem:

$$\arg\min_{a_o} \lambda_{ALB}\|a_o\|_1 + \frac{\mu_{ALB}}{2}\|a_o - a - b_a\|_2^2, \tag{S.4}$$

can be solved by:

$$a_o = \text{SoftThreshold}(a + b_a, \tfrac{\lambda_{ALB}}{\mu_{ALB}}), \tag{S.5}$$

where the function SoftThreshold is defined as:

$$\text{SoftThreshold}(x, \theta) = \text{sign}(x) \cdot \max(|x| - \theta, 0). \tag{S.6}$$

Similarly, the subproblem:

$$\arg\min_{\boldsymbol{a}_{TV}} \ \lambda_{TV}\|\boldsymbol{a}_{TV}\|_1 + \frac{\mu_{TV}}{2}\|\boldsymbol{a}_{TV} - \nabla a - \boldsymbol{b}_{TV}\|_2^2, \tag{S.7}$$

can be solved through:

$$\boldsymbol{a}_{TV} = \text{SoftThreshold}(\nabla a + \boldsymbol{b}_{TV}, \tfrac{\lambda_{TV}}{\mu_{TV}}). \tag{S.8}$$

Subsequently, we need to solve:

$$\arg\min_{a,d} \ \|\mathbb{I}[a > 0] - \mathbb{I}[d > 0]\|_1. \tag{S.9}$$

which aims to enforce that the albedo function and the depth function share the same support. To achieve this, we adopt a masking strategy where one of the functions is used to suppress spurious non-zero elements in the other. Since the albedo function is progressively refined during iterations, it provides a more reliable indicator of the support of the hidden object. Accordingly, we use the albedo function as a mask to constrain the depth function. For simplicity, we denote this operation by $\mathcal{P}_a$, and the updated depth function d is expressed as $\mathcal{P}_a(d)$. This support alignment can also be extended by replacing zero with a threshold value, which often yields more accurate reconstructions in practice.

Finally, we update the auxiliary variables b_a and $\boldsymbol{b}_{TV}$ directly through:

$$\begin{aligned} b_a &= b_a + a - a_o \\ \boldsymbol{b}_{TV} &= \boldsymbol{b}_{TV} + \nabla a - \boldsymbol{a}_{TV}. \end{aligned} \tag{S.10}$$

By repeating the above processes described in Eq. S.3 to Eq. S.10, we can obtain the reconstruction of the albedo and depth functions. Before giving the final output, we further take the square root of the albedo to enhance the reconstruction quality.

A pseudocode of the proposed reconstruction pipeline is provided in Alg. S.1. To accelerate the reconstruction process, we initialize the albedo and depth functions using the QFT method [2] as a^0 and d^0, rather than setting them to zero. For the variables inteoduced by the split Bregman method, we initialize them with zero values as a_o^0, $\boldsymbol{a}_{TV}^0$, b_a^0 and $\boldsymbol{b}_{TV}^0$.

S.1.2 Choice of the parameters

In this subsection, we discuss how to select the parameters. In addition to the scale parameter set S, there are four other parameters λ_{ALB}, μ_{ALB}, λ_{TV} and μ_{TV} introduced through the regularization terms and the split Bregman method.

To determine the scale parameter set S, we first determine a fundamental scale parameter s that controls the spread of the wavefront, defined as in the QFT method:

$$s = \max\left(\frac{l}{\sqrt{4\pi N}}, \frac{1}{4}\sqrt{\frac{c\delta t^2 N_t}{n\pi}}\right), \tag{S.11}$$

where l is the length of the scanning region and N denotes the number of scanning points in each dimension. The term c represents the light speed, δ_t is the time resolution of the detection device, and N_t is the time bins used for reconstruction. The constant n balances the noise and resolution, which is set as 0.1 in our experiments. This value can be fine-tuned around its theoretical estimate to improve reconstruction quality. The set of scale parameters is then obtained by adding perturbations to the fundamental value.

The number of scale parameters and the perturbation values depend on the complexity of the problem. For instance, in the regular confocal measurement setting, we typically use two scale parameters s and $s + 1 \times 10^{-7}$ for reconstruction. For more complex measurement settings, we usually employ more than three scale parameters. Except for s and $s + 1 \times 10^{-7}$, we often include $s + 1 \times 10^{-3}$ or $s + 1 \times 10^{-2}$ to the set.

Algorithm S.1 Pseudocode of the proposed reconstruction pipeline

Require: The scale parameter set S and corresponding aggregated measurements ϕ_s. Initializations a^0, d^0, a_o^0, $\boldsymbol{a}_{TV}^0$, b_a^0 and $\boldsymbol{b}_{TV}^0$.

Ensure: Two-dimensional functions a and d.

1: **for** $n = 0, 1, \ldots, N_{iter} - 1$ **do**

2: Update a and d

$$(a^{n+1}, d^{n+\frac{1}{2}}) = \arg\min_{a,d} \sum_{s\in S} \|\mathcal{F}_s(a,d) - \phi_s\|_2^2 + \frac{\mu_{ALB}}{2}\|a_o^n - a - b_a^n\|_2^2 + \frac{\mu_{TV}}{2}\|\boldsymbol{a}_{TV}^n - \nabla a - \boldsymbol{b}_{TV}^n\|_2^2$$

3: Update a_o

$$a_o^{n+1} = \arg\min_{a_o} \ \lambda_{ALB}\|a_o\|_1 + \frac{\mu_{ALB}}{2}\|a_o - a^{n+1} - b_a^n\|_2^2$$

4: Update $\boldsymbol{a}_{TV}$

$$\boldsymbol{a}_{TV}^{n+1} = \arg\min_{\boldsymbol{a}_{TV}} \ \|\boldsymbol{a}_{TV}\|_1 + \frac{\mu_{TV}}{2}\|\boldsymbol{a}_{TV} - \nabla a^{n+1} - \boldsymbol{b}_{TV}^n\|_2^2$$

5: Apply support alignment prior

$$d^{n+1} = \mathcal{P}_{a^{n+1}}(d^{n+\frac{1}{2}})$$

6: Update auxiliary variables

$$b_a^{n+1} = b_a^n + a^{n+1} - a_o^{n+1}$$
$$\boldsymbol{b}_{TV}^{n+1} = \boldsymbol{b}_{TV}^n + \nabla a^{n+1} - \boldsymbol{a}_{TV}^{n+1}$$

7: **end for**

8: $a = \sqrt{a^{N_{iter}}}, d = d^{N_{iter}}$

Additionally, the parameters λ_{ALB}, μ_{ALB}, and λ_{TV} are chosen within the ranges $[1, 10]$, $[20, 30]$, and $(0, 3]$, respectively, while μ_{TV} is fixed at 20. In the subproblem of updating the albedo a and depth d, we set the learning rates of the stochastic gradient descent method as 1×10^{-2} and 1×10^{-4}, respectively. The total number of iterations, N_{iter}, is fixed at 5 for all instances presented in this work.

In summary, although the proposed pipeline introduces additional parameters, most are constrained within narrow ranges or remain constant across different settings. Thus, they do not significantly increase the difficulty of applying the pipeline in real-world scenarios.

S.1.3 Details of the rendering

To evaluate the reconstruction accuracy of different methods, we generate synthetic data under the same setting as the real experiments, using publicly available rendering tools [3, 4, 5]. This subsection provides the details of the rendering process.

S.1.3.1 See-around-the-corner scenario

For the see-around-the-corner scenario, the scanning region on the relay wall spans $1.5 \times 1.5\text{m}^2$ with 256×256 scanning points. The USAF resolution chart is used as the hidden object, placed 1 m from the scanning wall. The photon travel distance per time bin is 0.0096 m, and the total number of photon samples is 1×10^6. For Fig. 5 in the main text, the signal is subsampled to 128×128 to accommodate GPU limitations in some state-of-the-arts methods.

S.1.3.2 See-through-the-medium scenario

For the simulated measurement for the see-through-the-medium scenario, the scanning region on the relay wall measures $0.8 \times 0.8, \text{m}^2$ with 256×256 scanning points. The scattering medium is a 2 cm-thick polyethylene foam. The USAF resolution chart is selected as the hidden object, placed 0.5 m behind the medium. The photon travel distance per time bin is set to 0.0096 m, and the number of samples is 1×10^6. To ensure compatibility with other methods, the signal used in Fig. 9 of the main text is subsampled to 128×128.

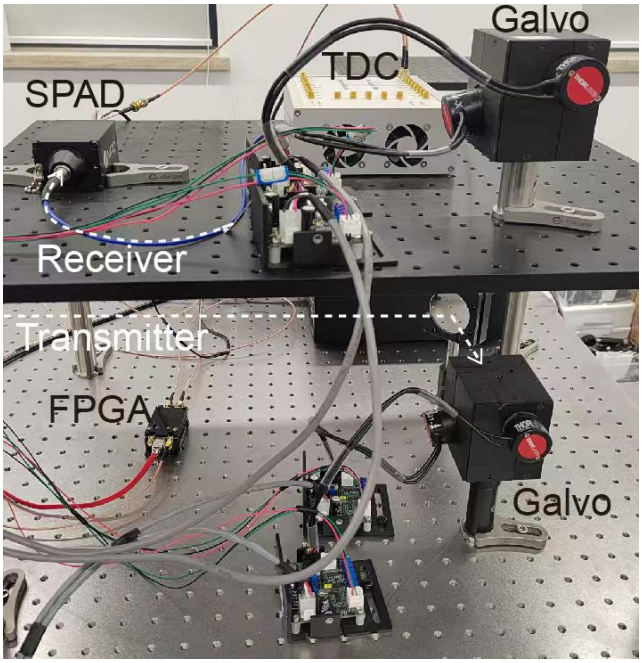

Figure S.1: Illustration of the experimental setup.

As the scattering process can be decomposed into two stages, propagation through the medium and free-space transport, we simulate the measurement in a stepwise manner. First, we render the free-space transport component using the publicly available tools.

Next, to simulate the effects of light diffusion through scattering media, we implement the image formation model proposed by Lindell and Wetzstein [6]. The forward model incorporates the diffusion kernel $\bar{\eta}$ that accounts for photon transport through a scattering medium. Derived from the diffusion equation with extrapolated boundary conditions [7], the kernel is expressed as:

$$\bar{\eta}(t, \mathbf{r}_0, \mathbf{r}_1) = \eta(t, \mathbf{r}_0, \mathbf{r}_1) * \eta(t, \mathbf{r}_0, \mathbf{r}_1), \tag{S.12}$$

where t is the time after laser pulse excitation, $\mathbf{r_0}$ and $\mathbf{r_1}$ represent points on two sides of the scattering media, and η represents the single-pass diffusion kernel which is defined as:

$$\begin{aligned}\eta\left(t, \mathbf{r_0}, \mathbf{r_1}\right) = & \frac{1}{2(4\pi Dc)^{3/2} t^{5/2}} \\ & \exp\left(-\mu_{\mathrm{a}} ct - \frac{\|\mathbf{r}_1 - \mathbf{r}_0\|_0^2}{4Dct}\right) \\ & \cdot \sum_{i=-\infty}^{\infty} \left[\left(z_{\mathrm{d}} - z_{+,i}\right) \exp\left(-\frac{\left(z_{\mathrm{d}} - z_{+,i}\right)^2}{4Dct}\right) \right. \\ & \left. - \left(z_{\mathrm{d}} - z_{-,i}\right) \exp\left(-\frac{\left(z_{\mathrm{d}} - z_{-,i}\right)^2}{4Dct}\right) \right].\end{aligned} \tag{S.13}$$

Here, $\mathbf{r}_0$ denotes the illumination and detection point on the surface of the scattering medium, $\mathbf{r}_1$ represents a point on the far side of the scattering medium. The parameter c is the speed of light in the medium, μ_a is the absorption coefficient, μ_s' is the reduced scattering coefficient, and $D = [3(\mu_a + \mu_s')]^{-1}$ is the diffusion coefficient. The thickness of the scattering medium is denoted by z_d, and z_e is the extrapolation distance accounting for refractive index mismatch at the medium-air interface. The depth at which incident photons are first scattered isotropically is given by $z_0 = 1/\mu_s'$. The terms $z_{+,i} = 2i\left(z_{\mathrm{d}} + 2z_{\mathrm{e}}\right) + z_0$ and $z_{-,i} = 2i\left(z_{\mathrm{d}} + 2z_{\mathrm{e}}\right) - 2z_{\mathrm{e}} - z_0$ represent the positions of the positive and negative dipole sources required to satisfy the extrapolated boundary conditions.

Finally, we convolve the diffusion kernel with the free-space transport signal using a 3D FFT to obtain the simulated measurement.

S.1.4 Details of the measurement

The experimental setup is illustrated in Fig. S.1, where a non-coaxial structure is employed to circumvent the saturation effects caused by the unexpected laser echoes. In the transmitter system, a pulsed laser beam (Femto YL-Green-10, YSL Photonics), operating at 515 nm, illuminates the target area with a pulse width of 235 fs and a repetition rate of 10 MHz. In the receiver system, a silicon-based single-photon avalanche diode (SPAD) with detection efficiency of 40% and temporal jitter of 50 ps (PDM, Micro Photon Devices), is utilized to collect the echo photons. The time-of-flight information is subsequently recorded by a time-to-digital converter (TDC) (Time Tagger Ultra, Swabian instruments). The galvo systems (GVS012/M, Thorlabs) in the transceiver are synchronized to perform raster scanning on the scattering medium or the relay wall. A customized field-programmable gate array (FPGA) is used as a gated module, allowing for arbitrary adjustment of the pulse width and temporal delay. Inspired by the auto-calibration method[8, 9], we adopt the confocal scanning mode and maintain a vertical misalignment of 13 cm in the experiment.

The regular confocal measurements with 512×512 and 1024×1024 scanning points (Figs. 2 and 6 in the main text) are generated using nearest-neighbor interpolation [10, 11, 12] from the original 256×256 scanning points measurements. This approach is used to highlight the superior performance of the proposed pipeline and to emphasize the importance of capturing and reconstructing signals at higher resolutions.

For the non-confocal reconstructions shown in Fig. 6 of the main text, the original measurements have 256×256. Each measurement is approximated as a confocal signal of the same size. To prevent the reconstruction from exceeding the boundary, we apply zero-padding around the approximated confocal signals corresponding to the letters "n" and "t," resulting in signals with 512×512 scanning points.

S.1.5 Simplification of the forward model under the see-through-the-medium scenario

As described in the main text, the forward model of the see-through-the-medium scenario can be decomposed into two parts: scattering through the medium and the free-space transportation. The general model can be expressed as:

$$\tau_u(\boldsymbol{x}, t) = \mathcal{T}_S \circ \mathcal{T}_F(\boldsymbol{x}, t), \tag{S.14}$$

where τ_u denotes the measurement, $\mathcal{T}_S$ represents the scattering process within the medium, and $\mathcal{T}_F$ models free-space propagation. Additionally, the symbol $\boldsymbol{x} \in \mathbb{R}^2$ denotes the confocal scanning point, and t denotes the time. The symbol $\circ$ denotes the composition of the operators. The three-point transport model can be employed to describe the free-space transportation part, which is the same model as the see-around-the-corner scenario. If the hidden object is located in the scattering medium, then the second part is neglected. In this section, we will further simplify the model of see-through-the-medium based on existing models and use numerical experiments to illustrate its effectiveness.

The forward model of scattering in a medium can be described by the diffusion approximation of the radiative transport equation [6, 13]. However, solving this equation in three-dimensional space requires excessive computation and memory. Moreover, existing methods adopt different forward models for different see-through-the-medium scenarios. For instance, when the hidden object lies behind foam, methods often use a two-stage model that introduces an anisotropic kernel [6, 14] (see Eqs. S.12 and S.13). In contrast, when the hidden object is embedded within the scattering medium, light propagation is modeled directly with the diffusion equation, omitting the free transport process [13, 15]. This inconsistency makes it difficult to design a unified and efficient reconstruction algorithm for general scenarios, forcing observers to rely on different algorithms for different cases and thereby limiting the overall practicality of the technique.

Therefore, we need to further simplify the forward model. Similar to the see-around-the-corner scenario, we formulate the forward model of the see-through-the-medium scenario as:

$$\mathcal{T}_S \circ \mathcal{T}_F(\boldsymbol{x}, t) = \int_\Omega \frac{G(\boldsymbol{x}, \boldsymbol{y})}{r^m} f(\boldsymbol{y}) \delta(2r - ct) d\boldsymbol{y}, \tag{S.15}$$

where r is the distance between points $\boldsymbol{x}$ and $\boldsymbol{y}$. The function f represents the volumetric albedo of the hidden object, and Ω is a domain that contains the region of interest.

The function $G(\boldsymbol{x}, \boldsymbol{y})$ and the parameter m describe the geometric falloff of light intensity. According to the Beer-Lambert law, the function G can be expressed as a function of $e^{-\beta \|(\boldsymbol{x},0)-\boldsymbol{y}\|_2}$.However, since we consider only weak scattering in this manuscript and the hidden objects are located close to the scattering medium, we neglect this term for further simplification.

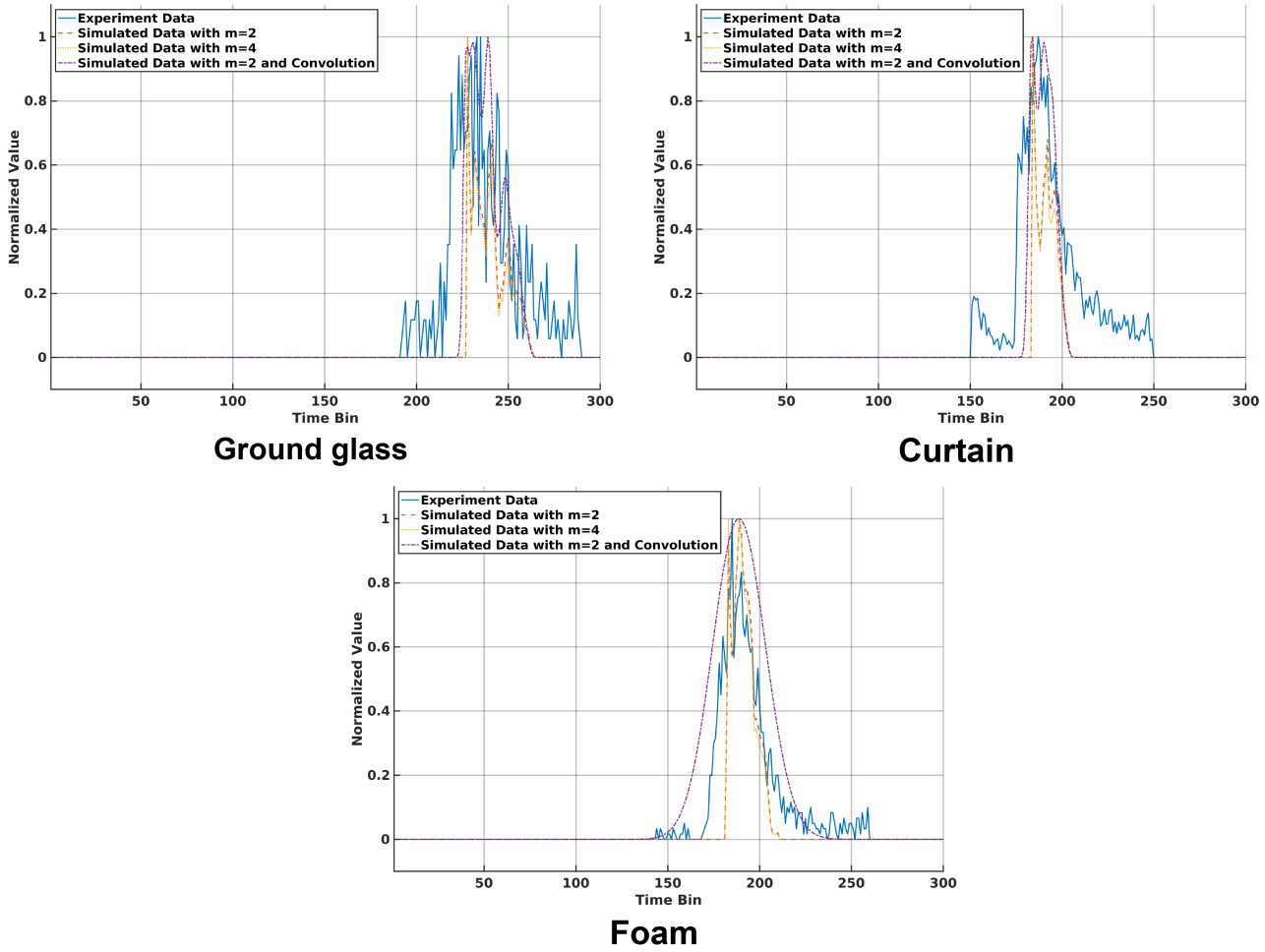

Figure S.2: Comparison of rendered data from different forward models with real measurement.

In Fig. S.2, we compare the simulated data with the measurements. Specifically, we examine results generated using $m = 2$, $m = 4$, and the full forward model with the kernel defined in Eqs. S.12 and S.13. The comparisons show that the three forward models produce very similar outputs. Although the data rendered from the full model appears smoother, it requires significantly more time and memory to compute the convolution.

By contrast, the models with $m = 2$ and $m = 4$ are nearly identical, differing only in minor details. Overall, the $m = 2$ model is generally closer to the measurements in most cases. Moreover, it introduces less noise when multiplied by the measurements during the aggregation process.

Therefore, considering both computational efficiency and reconstruction quality, we adopt the following forward model for the see-through-the-medium scenario:

$$\mathcal{T}_S \circ \mathcal{T}_F(\boldsymbol{x}, t) = \int_\Omega \frac{1}{r^2} f(\boldsymbol{y}) \delta(2r - ct) d\boldsymbol{y}. \tag{S.16}$$

S.2 Supplementary Results

S.2.1 Complete comparisons of the experiments shown in the main text

In this subsection, we present detailed comparisons of the figures shown in the main text. All methods are implemented in PyTorch. If a method cannot run on a single GPU with 24 GB of memory, it is executed on a CPU server with 1 TB of memory.

The full comparisons of Figs. 2 and 6 in the main text are displayed in Figs. S.3 and S.5. Their corresponding depth reconstructions are shown in Figs. S.4 and S.6, respectively. Furthermore, we compare

the reconstructed intensity along the same curve of the smallest resolution bar shown in the last row of Fig. S.5. Existing methods fail to clearly separate the bars, whereas the proposed pipeline produces reconstructions with zero values correctly filled within the bars, thereby outperforming existing techniques. In comparison with existing approaches, the proposed method not only achieves greater efficiency, as discussed in the main text, but also delivers substantially better reconstructions in both scenarios.

In Fig. S.7, we present a complete comparison corresponding to Fig. 3 in the main text. In the first setting, the letter T is placed outside a 2 cm-thick polyethylene foam, while the second shows the letter "O" beyond a curtain. Across both scenarios, the proposed pipeline consistently produces faithful reconstructions with substantially clearer backgrounds, demonstrating its robustness in handling general NLOS imaging tasks.

Figure S.8 presents a comprehensive comparison corresponding to Fig. 7 in the main text. The reconstructions produced by the proposed pipeline exhibit the highest imaging quality, demonstrating its superior performance.

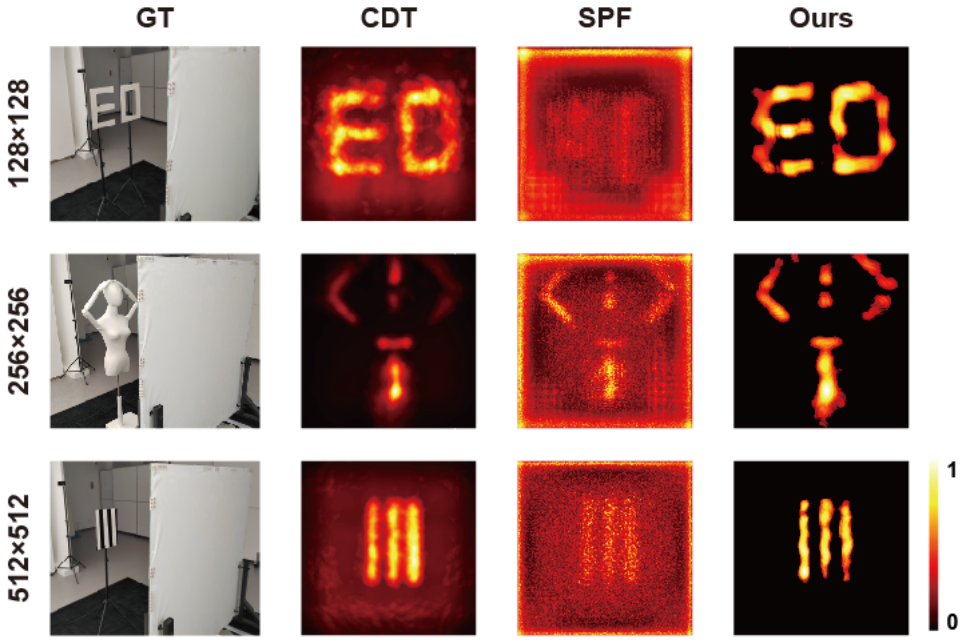

Figure S.3: Complete comparison of albedo reconstructions of the see-through-the-medium scenario.

S.2.2 Results on public datasets

We first evaluate the performance of the proposed pipeline for looking through a medium using the dataset provided by the CDT method [6]. In this scenario, the hidden objects are obscured by a 2.54-cm-thick piece of polyurethane foam. The signals are captured using a 32×32 scanning grid, though the size of the scanning region differs from previous settings. Figure S.9 illustrates the reconstructions provided by different methods. The proposed pipeline produces reconstructions not only significantly faster but also with noticeably higher quality.

We then use the Stanford dataset [10] to evaluate the performance of our pipeline in the see-around-the-corner scenario. The measurement region on the relay wall spans 2×2 m^2 and contains 512×512 scanning points. To test the pipeline's robustness to measurement noise and scene complexity, we select instances with the shortest and longest exposure times. The complete comparison of Fig. 8 in the main text is shown in Fig. S.10. Among these, our proposed method delivers higher-quality reconstructions, characterized by a cleaner background and finer detail.

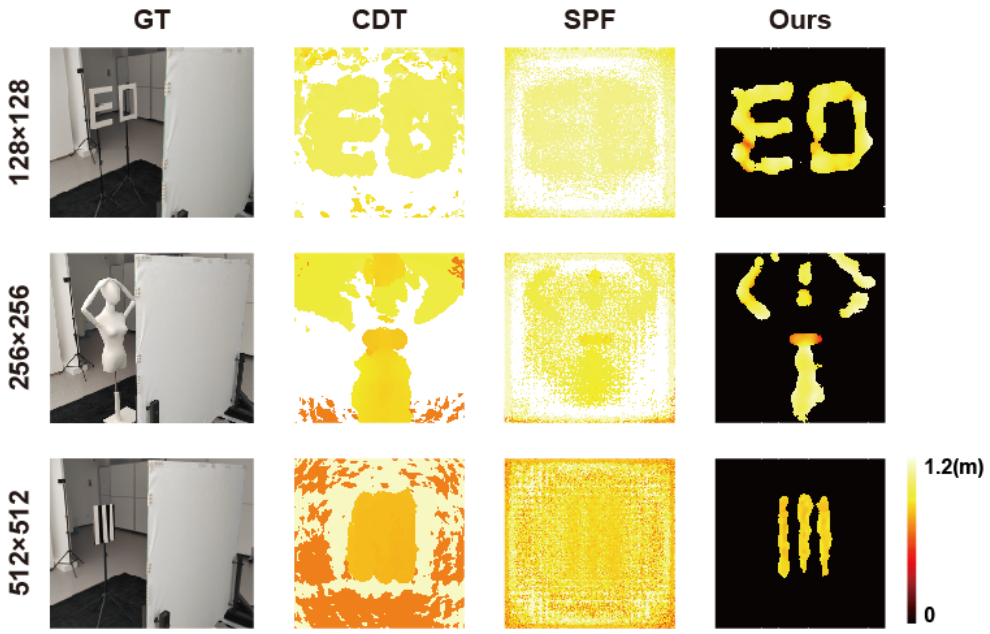

Figure S.4: Complete comparison of depth reconstructions of the see-through-the-medium scenario.

References

[1] Tom Goldstein and Stanley Osher. The split bregman method for l1-regularized problems. *SIAM journal on imaging sciences*, 2(2):323–343, 2009.

[2] Yijun Wei, Jianyu Wang, Leping Xiao, Zuoqiang Shi, Xing Fu, and Lingyun Qiu. Fast and memory-efficient non-line-of-sight imaging with quasi-fresnel transform, 2025.

[3] Diego Royo, Jorge García, Adolfo Muñoz, and Adrian Jarabo. Non-line-of-sight transient rendering. *Computers & Graphics*, 107:84–92, 2022.

[4] Diego Royo, Miguel Crespo, and Jorge Garcia-Pueyo. mitransient. `https://github.com/diegoroyo/mitransient`, 2023.

[5] Diego Royo and Pablo Luesia-Lahoz. y-tal.

[6] David B Lindell and Gordon Wetzstein. Three-dimensional imaging through scattering media based on confocal diffuse tomography. *Nature communications*, 11(1):4517, 2020.

[7] Richard C Haskell, Lars O Svaasand, Tsong-Tseh Tsay, Ti-Chen Feng, Matthew S McAdams, and Bruce J Tromberg. Boundary conditions for the diffusion equation in radiative transfer. *Journal of the Optical Society of America A*, 11(10):2727–2741, 1994.

[8] Zhengqing Pan, Ruiqian Li, Tian Gao, Zi Wang, Siyuan Shen, Ping Liu, Tao Wu, Jingyi Yu, and Shiying Li. Onsite non-line-of-sight imaging via online calibration. *IEEE Photonics Journal*, 14(5):1–11, 2022.

[9] Leping Xiao, Jianyu Wang, Yi Wang, Ziyu Zhan, Zuoqiang Shi, Lingyun Qiu, and Xing Fu. Fast non-line-of-sight imaging with hybrid super-resolution network over 18 m. *IEEE Transactions on Computational Imaging*, 2024.

[10] David B Lindell, Gordon Wetzstein, and Matthew O'Toole. Wave-based non-line-of-sight imaging using fast fk migration. *ACM Transactions on Graphics (ToG)*, 38(4):1–13, 2019.

[11] Xiaochun Liu, Sebastian Bauer, and Andreas Velten. Phasor field diffraction based reconstruction for fast non-line-of-sight imaging systems. *Nature communications*, 11(1):1645, 2020.

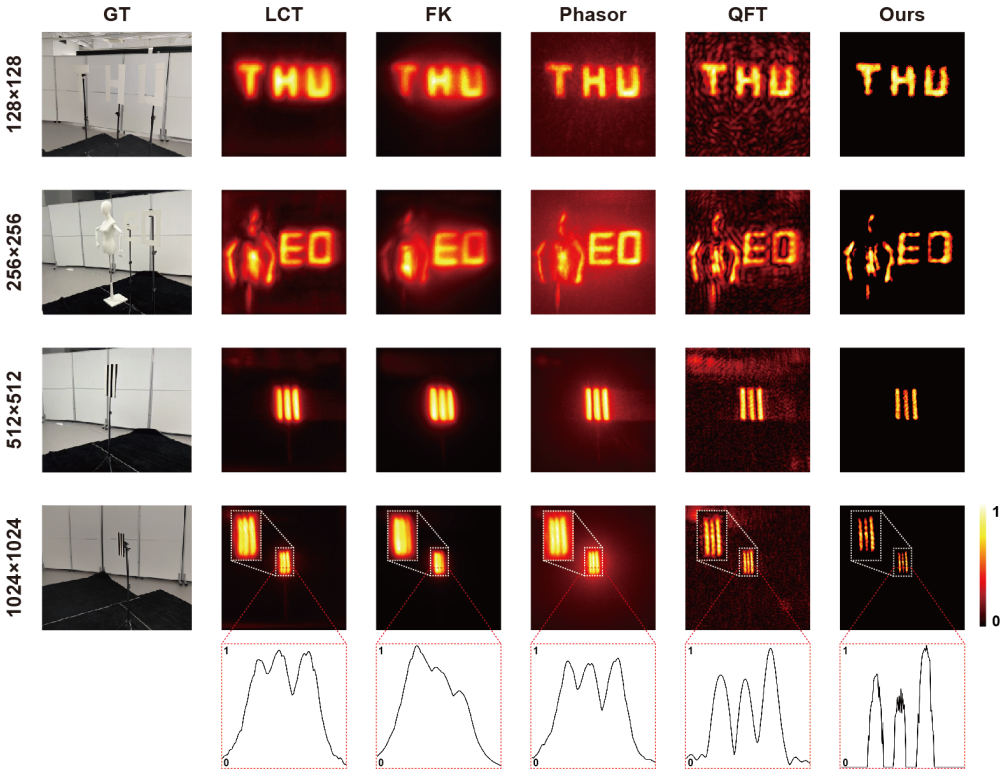

Figure S.5: Complete comparison of albedo reconstructions of the see-around-the-corner scenario.

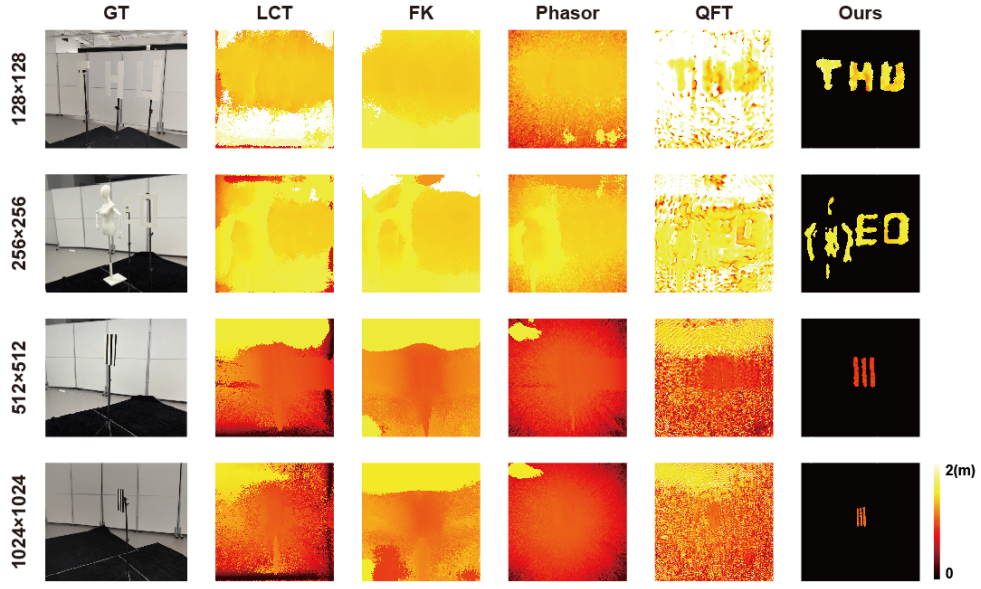

Figure S.6: Complete comparison of depth reconstructions of the see-around-the-corner scenario.

[12] Jianyu Wang, Xintong Liu, Leping Xiao, Zuoqiang Shi, Lingyun Qiu, and Xing Fu. Non-line-of-sight imaging with signal superresolution network. In *Proceedings of the IEEE/CVF Conference on Computer Vision and Pattern Recognition*, pages 17420–17429, 2023.

[13] Dongyu Du, Xin Jin, Rujia Deng, Jinshi Kang, Hongkun Cao, Yihui Fan, Zhiheng Li, Haoqian Wang, Xiangyang Ji, and Jingyan Song. A boundary migration model for imaging within volumetric scattering

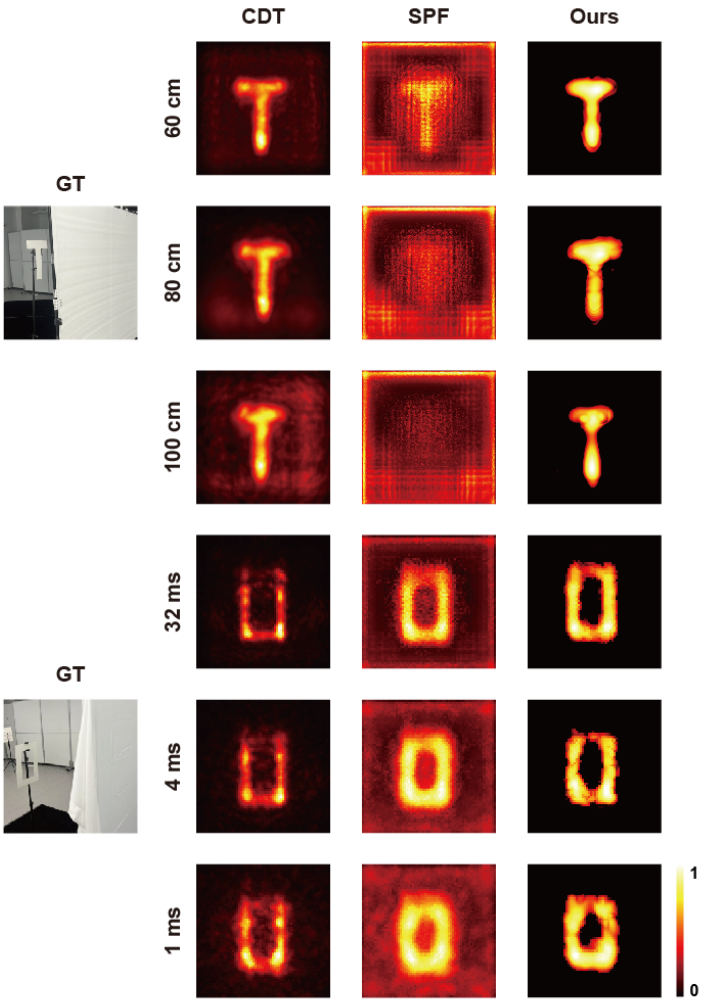

Figure S.7: Complete comparison of different settings of the see-through-the-medium scenario.

media. *Nature Communications*, 13(1):3234, 2022.

[14] Jianwei Zeng, Wei Li, Yijun Zhou, and Feihu Xu. Single-photon 3d imaging of room-scale scenes through scattering media. *Optics Express*, 32(23):40706–40718, 2024.

[15] Dongyu Du, Xin Jin, and Rujia Deng. Non-confocal 3d reconstruction in volumetric scattering scenario. *IEEE Transactions on Computational Imaging*, 9:732–744, 2023.

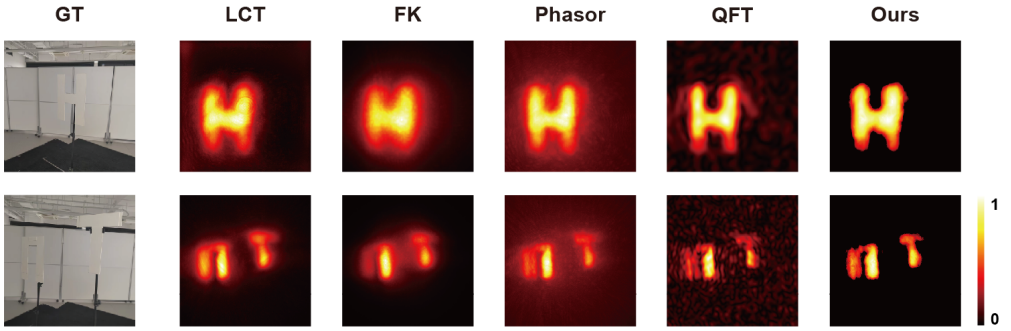

Figure S.8: Complete comparison of non-confocal measurement under the see-around-the-corner scenario.

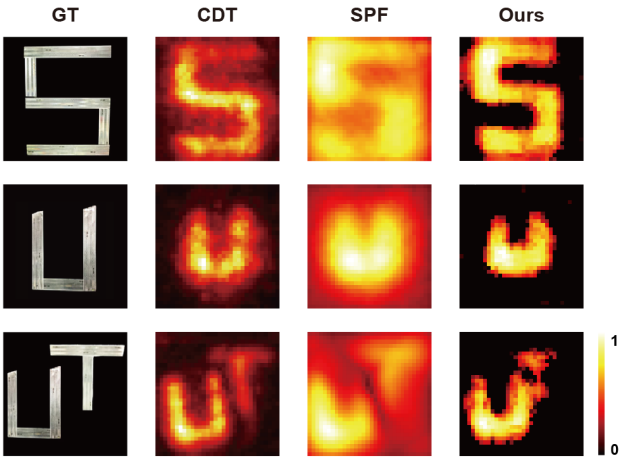

Figure S.9: Reconstructions of the public dataset in the see-through-the-medium scenario.

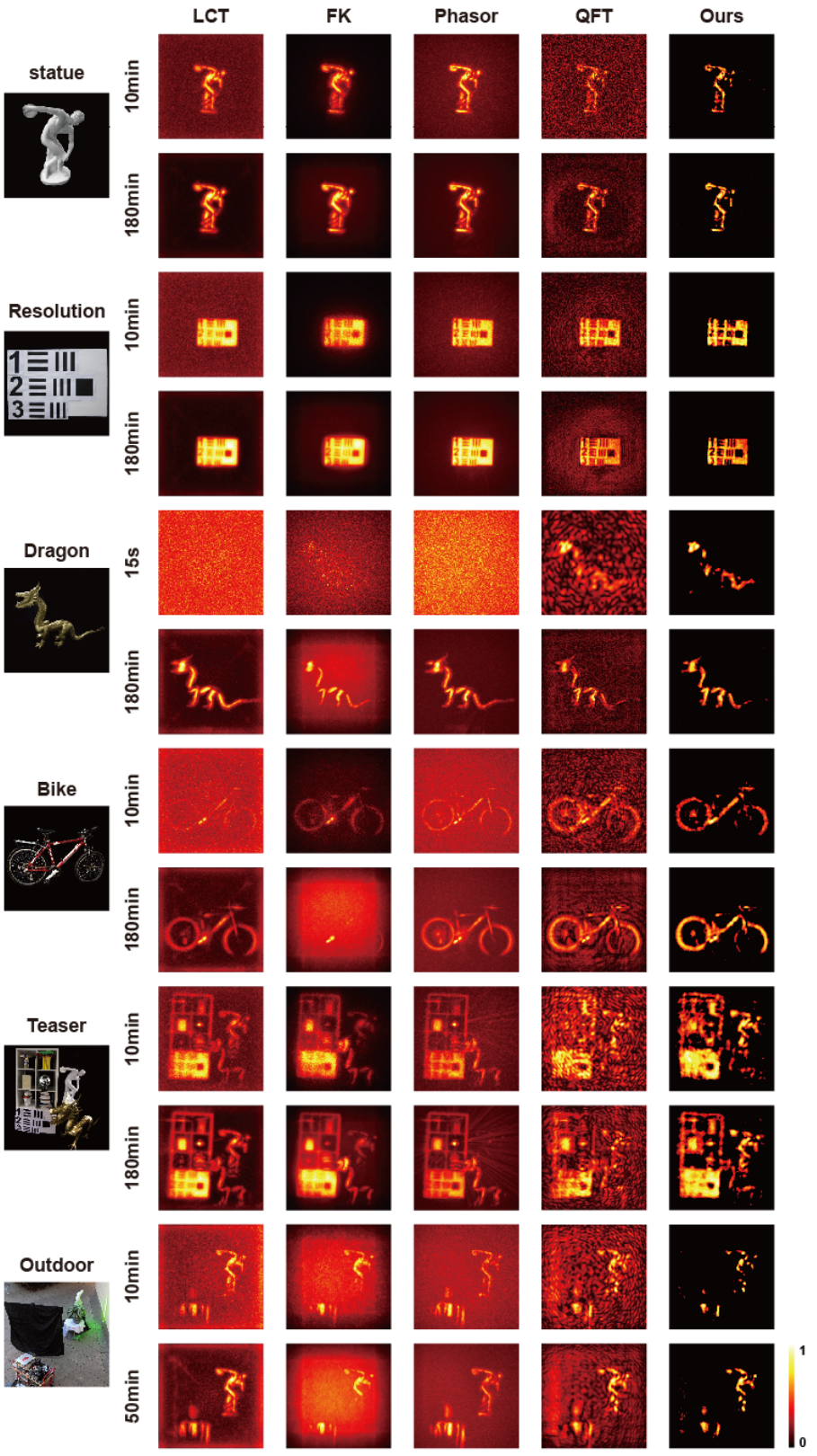

Figure S.10: Reconstructions of the public dataset in the see-around-the-corner scenario.